Accelerated Electromagnetic Transient (EMT) Equivalent Model of Solid-State Transformer

Chenxiang Gao, Moke Feng, Jiangping Ding, Hang Zhang, Jianzhong Xu, *Senior Member*, *IEEE*, Chengyong Zhao, *Senior Member*, *IEEE,* Zixin Li, *Member*, *IEEE,* and Gen Li, *Member, IEEE*

[1]*Abstract*— **Accurate and efficient electromagnetic transient (EMT) simulation of various types of solid-state transformers (SST) is extremely time-consuming due to the complex module structure, flexible topology connections, large number of electrical nodes and simulation time-steps limited in the range of micro-seconds. Therefore, it is urgent to develop the EMT equivalent modelling and fast simulation of SSTs for system level studies. Taking the modular multilevel converter (MMC) based SST as an example, this paper proposes an accelerated EMT model which focuses on the equivalence of the dual active bridge (DAB) based high-frequency link (HFL) in the SST. Compared with the existing algorithms, two critical factors of the proposed method that contribute the most to the efficiency improvement are the preprocessing of the nodal admittance equation and the conversion of the short-circuit admittance parameters. The proposed model is verified in PSCAD/EMTDC by comparing it with the detailed EMT model. The results show that the accelerated model is one to two orders of magnitude faster than the detailed model without sacrificing the accuracy. The experiment validation also confirms the validity of the proposed model.**

Index Terms— **Electromagnetic transient (EMT) simulation, accelerated equivalent model, solid-state transformer (SST), preprocessing, parameter conversion.**

I. INTRODUCTION

Solid-state transformer (SST), which is able to realize the transformation of multiple voltage levels and integration of various energy sources, can play an important role in achieving a low-carbon smart grid [1]-[5]. To meet the needs of different application scenarios, there are various power module (PM) structures of SSTs. Specifically, cascaded H-bridge (CHB) and modular multilevel converter (MMC) can be deployed in the medium-voltage (MV) side as AC/DC converters, while dual active bridge (DAB), multiple active bridge (MAB) and single active bridge (SAB) can be used in the low-voltage (LV) side as DC/DC converters [6]-[11]. Moreover, multiple connection configurations of the PMs

have been proposed to address the dilemma of increasing the converter capacity and reducing the device rating [12], [13], such as the input-series-output-parallel (ISOP), input-series-output-series (ISOS), input-parallel-output-parallel (IPOP) and input-parallel-output-series (IPOS).
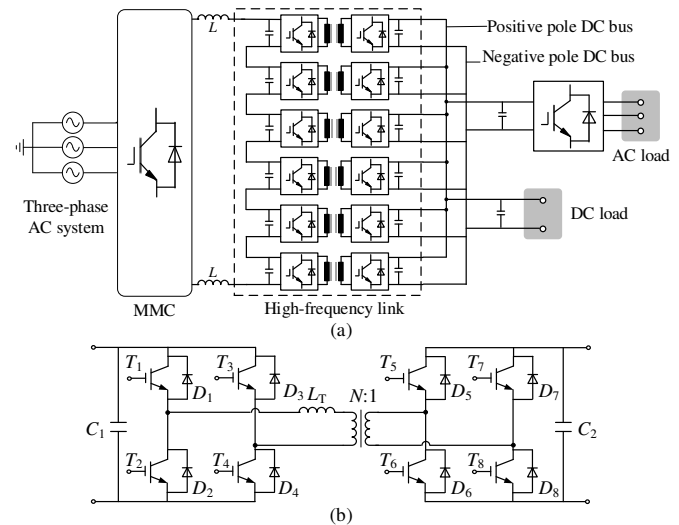

Fig. 1. MMC-based SST. (a) Converter structure; (b) DAB PM structure.

Combining the advantages of MMCs and the ISOP configuration, a typical MMC based SST is presented in [14], as shown in Fig. 1(a). Its high-frequency link (HFL) is based on the DAB PM shown in Fig. 1(b). The large number of sub-modules (SMs) leads to a high-order of admittance matrix in the electromagnetic transient (EMT) simulation using fully detailed models (DMs), which requires the simulation time-steps to be in the range of microseconds due to the power electronic switches and high-frequency isolation transformers [15], [16]. Hence, both MMC and HFL face very urgent needs for EMT equivalent modelling and fast simulation.

Recently, the research on the accelerated equivalent models (EMs) of MMCs has been relatively mature [17]-[20]. Specifically, the EMs in [19] and [20] create a single- or multi-port Norton equivalent circuit by recursively eliminating internal nodes. Their modelling methods show good acceleration and accuracy without losing the information of internal nodes. However, these methods are designed for MMCs and therefore, cannot be directly applied to the HFL, because the topologies and connection configurations of PMs are more complicated in HFLs.

To bridge the research gap of developing acceleration models for HFLs, efforts have been made in the open literature. The accelerated equivalent mathematical model for the SAB

PM has been established in [21], which is based on the accurate mode division and complex high-order integration algorithm. References [22] and [23] propose average models for SSTs, which can highly improve the simulation speed. However, these models sacrifice the capability of describing the transient behaviors inside PMs.

In the newly reported high-speed equivalent modelling algorithm of CHB-based SST [24], the HFL is represented by a two single-port circuit through eliminating the internal nodes and discretizing the isolation transformer into two-port Norton circuits. The EM shows good performances in the aspects of efficiency, accuracy and scalability. However, it needs to conduct the approximation of circuit equations, which may result in additional errors. Moreover, there are still several matrix inversion operations in the calculation process of each time-step, therefore the equivalent algorithm still has room for further speed-up.

This paper proposes an accelerated EMT equivalent modelling method focusing on the HFL. The developed models are compared against detailed models and experimental results. Very high accuracy along with a speedup of 2 to 3 orders of magnitude can be achieved.

II. THE PROPOSED ACCELERATED MODELLING METHOD

Different from the single-port SMs such as half-bridge (HB) and full-bridge (FB) in MMCs, there are at least two ports in the SST PMs. Meanwhile, the connection configurations of SST PMs are varied, which include four typical connections, i.e., ISOP, ISOS, IPOS, IPOP, and their nested forms [12], [13].

The topology of the two-port PM is shown in Fig. 2, where the subscripts "IN" and "OUT" represent the input and output ports.
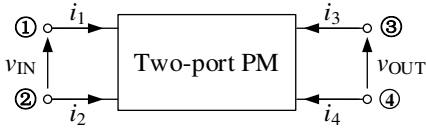

Fig. 2. Two-port PM topology.

Due to the isolated transformer, the two-port characteristics, i.e., $i_1+i_2=0$ and $i_3+i_4=0$, are satisfied in mathematics [20]. For such isolated networks, 4 types of port parameters are defined in [24] to describe the relationship between the currents and voltages of the input and output ports, as listed in the first column of Table I. Among them, the short-circuit admittance parameters are closely related to the node admittance matrix of the system and can be converted to the other three types.

TABLE I
TYPE OF PARAMETERS FOR DIFFERENT CONNECTION CONFIGURATIONS

Type of port parameters	Common variables	Connection configurations
Hybrid parameters, H	i_{IN} and v_{OUT}	ISOP
Open-circuit impedance parameters, Z	i_{IN} and i_{OUT}	ISOS
Inverse hybrid parameters, G	v_{IN} and i_{OUT}	IPOS
Short-circuit admittance parameters, Y	v_{IN} and v_{OUT}	IPOP

Taking the hybrid parameters as an example, the PM port equation can be written as (1), where h_{11}, h_{12}, h_{21}, h_{22} are the hybrid parameters, H is the hybrid parameter matrix, v_{IN_OC} and i_{OUT_SC} are the independent sources.

$$\begin{bmatrix} v_{IN} \\ i_{OUT} \end{bmatrix} = \begin{bmatrix} h_{11} & h_{12} \\ h_{21} & h_{22} \end{bmatrix} \cdot \begin{bmatrix} i_{IN} \\ v_{OUT} \end{bmatrix} + \begin{bmatrix} v_{IN\_OC} \\ i_{OUT\_SC} \end{bmatrix}$$
$$\triangleq H \cdot \begin{bmatrix} i_{IN} \\ v_{OUT} \end{bmatrix} + \begin{bmatrix} v_{IN\_OC} \\ i_{OUT\_SC} \end{bmatrix}. \quad (1)$$

It is known that all PMs connected in the ISOP configuration share the common input-port current i_{IN} and output-port voltage v_{OUT}. Hence, the port equation of the HFL can be obtained as (2), by directly summing the corresponding parameters in the hybrid parameter port equations of all PMs.

$$\begin{bmatrix} v_{IN}^{tot} \\ i_{OUT}^{tot} \end{bmatrix} = \begin{bmatrix} \sum_{i=1}^{N} v_{IN}^{i} \\ \sum_{i=1}^{N} i_{OUT}^{i} \end{bmatrix} = \sum_{i=1}^{N} H_i \cdot \begin{bmatrix} i_{IN} \\ v_{OUT} \end{bmatrix} + \begin{bmatrix} \sum_{i=1}^{N} v_{IN\_OC}^{i} \\ \sum_{i=1}^{N} i_{OUT\_SC}^{i} \end{bmatrix},$$
$$\triangleq \begin{bmatrix} h_{tot\_11} & h_{tot\_12} \\ h_{tot\_21} & h_{tot\_22} \end{bmatrix} \cdot \begin{bmatrix} i_{IN} \\ v_{OUT} \end{bmatrix} + \begin{bmatrix} v_{IN\_OC}^{tot} \\ i_{OUT\_SC}^{tot} \end{bmatrix} \quad (2)$$

where N is the number of PMs, v_{IN}^{tot} and i_{OUT}^{tot} are the input-port voltage and output-port current of the converter.

However, it is not easy to directly obtain the hybrid parameters of SST PMs. Fortunately, the hybrid parameters can be converted by (3) using the short-circuit admittance parameters, which are defined in (4).

$$\begin{bmatrix} v_{IN} \\ i_{OUT} \end{bmatrix} = \begin{bmatrix} \dfrac{1}{y_{11}} & -\dfrac{y_{12}}{y_{11}} \\ \dfrac{y_{21}}{y_{11}} & \dfrac{y_{11}y_{22}-y_{12}y_{21}}{y_{11}} \end{bmatrix} \cdot \begin{bmatrix} i_{IN} \\ v_{OUT} \end{bmatrix} + \begin{bmatrix} \dfrac{1}{y_{11}} j_{S1} \\ \dfrac{y_{21}}{y_{11}} j_{S1} - j_{S2} \end{bmatrix}, (3)$$

$$\begin{bmatrix} i_{IN} \\ i_{OUT} \end{bmatrix} = \begin{bmatrix} y_{11} & y_{12} \\ y_{21} & y_{22} \end{bmatrix} \cdot \begin{bmatrix} v_{IN} \\ v_{OUT} \end{bmatrix} + \begin{bmatrix} j_{S1} \\ j_{S2} \end{bmatrix} \triangleq Y \cdot \begin{bmatrix} v_{IN} \\ v_{OUT} \end{bmatrix} + \begin{bmatrix} j_{S1} \\ j_{S2} \end{bmatrix}, (4)$$

where y_{11} and y_{22} represent the input-admittance of the two ports, y_{12} and y_{21} represent transfer-admittances, and Y is the short-circuit admittance matrix, j_{S1} and j_{S2} represent the independent current sources of the two ports [24]. Since the SST PM is composed of passive components, the port equation in (4) meets the reciprocity characteristics, i.e., $y_{12}=y_{21}$, which is proved in the next section.

Similar to the equivalent model of the isolated transformer given in [16], the port equations using short-circuit admittance parameters in (4) have actual physical meanings as illustrated in the equivalent circuit in Fig. 3.
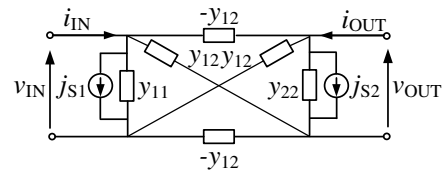

Fig. 3. Two-port equivalent circuit using short-circuit admittance parameters.

To facilitate the EMT simulation, the port equations of HFL in (2) need to be reversed to the short-circuit admittance parameters. Furthermore, once the external information i_{IN} and v_{OUT} are calculated at each simulation time-step of the

EMT solver, v_{IN} and i_{OUT} of each SST PMs can be directly calculated by (1).

Noted that, the method is also applied to other connection configurations. According to the common variables shared by SST PMs, the type of the port parameters can be selected as listed in Table I. The port parameter matrix of HFL, i.e., Z, G or Y, is the sum of the corresponding parameter matrices of PMs. This is also the case for the independent sources. Besides, when the port number of PMs increase, such as MAB, the order of the parameter matrix will increase accordingly.
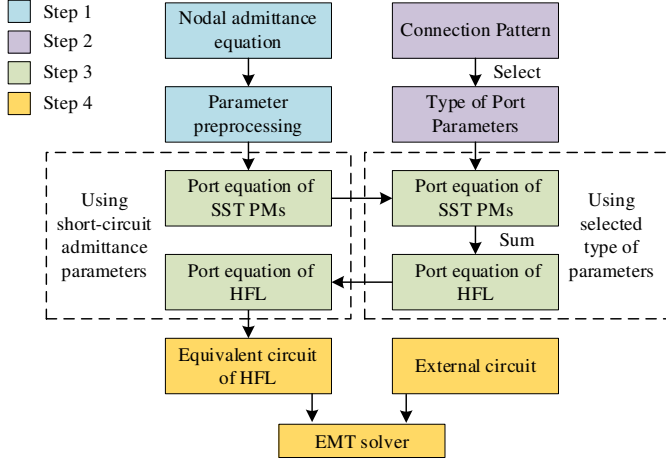

Fig. 4. The procedures of the accelerated equivalent modelling method.

The procedures of the proposed accelerated EMT modelling method of SST are given in Fig. 4, which include the following 4 steps:

Step 1: Obtain the port equation using short-circuit admittance parameters of SST PMs through parameter preprocessing of the nodal admittance equation. This progress is complicated and will be carefully discussed in the following Section III.

Step 2: Select the type of port parameters according to the SST connection pattern.

Step 3: Calculate the port equation of HFL by the conversion between the short-circuit admittance parameters and the selected type of parameters.

Step 4: Form the equivalent circuit of HFL using the short-circuit admittance parameters. Then the EMT solver is used to solve the full network combined with the external circuit.

A portion of this method has been presented in [26], which is significantly improved in this paper. In addition, the equivalent modelling method of the blocking mode can be effectively solved by calling the sub-function of the diode model from the EMT solver [24], which is out of the scope of this paper.

III. OBTAIN THE PORT EQUATION OF THE POWER MODULE

In this section, a method is proposed to obtain the port equation of SST PMs using short-circuit admittance parameters. Different from the equivalent modelling method in [24], the preprocessing of the nodal admittance equation is used to minimize the algebraic operations. Herein, the study focuses on the DAB PM, but this method is also applicable to other types of SST PMs, as discussed in Section IV.

A. Relationship between the Nodal Admittance Equation and the Port Equation using Short-circuit Admittance Parameters

As for the isolated two-port network shown in Fig. 2, the complete matrix expressions of the port characteristics are

$$\begin{bmatrix} 1 & 0 \\ -1 & 0 \\ 0 & 1 \\ 0 & -1 \end{bmatrix} \cdot \begin{bmatrix} i_{\text{IN}} \\ i_{\text{OUT}} \end{bmatrix} = \begin{bmatrix} i_1 \\ i_2 \\ i_3 \\ i_4 \end{bmatrix}, \quad \begin{bmatrix} 1 & -1 & 0 & 0 \\ 0 & 0 & 1 & -1 \end{bmatrix} \cdot \begin{bmatrix} v_1 \\ v_2 \\ v_3 \\ v_4 \end{bmatrix} = \begin{bmatrix} v_{\text{IN}} \\ v_{\text{OUT}} \end{bmatrix}, (5)$$

where v_1-v_4 and i_1-i_4 are the voltages and injection currents of the 4 terminals of the two-port network.

Combine (4) and (5), the relationship between the nodal admittance equation and the port equation using short-circuit admittance parameters is given in (6).

$$\begin{bmatrix} i_1 \\ i_2 \\ i_3 \\ i_4 \end{bmatrix} = \begin{bmatrix} 1 & 0 \\ -1 & 0 \\ 0 & 1 \\ 0 & -1 \end{bmatrix} \cdot \begin{bmatrix} y_{11} & y_{12} \\ y_{21} & y_{22} \end{bmatrix} \begin{bmatrix} 1 & -1 & 0 & 0 \\ 0 & 0 & 1 & -1 \end{bmatrix} \begin{bmatrix} v_1 \\ v_2 \\ v_3 \\ v_4 \end{bmatrix} + \begin{bmatrix} 1 & 0 \\ -1 & 0 \\ 0 & 1 \\ 0 & -1 \end{bmatrix} \cdot \begin{bmatrix} j_{\text{S1}} \\ j_{\text{S2}} \end{bmatrix}$$

$$= \begin{bmatrix} y_{11} \cdot \begin{bmatrix} 1 & -1 \\ -1 & 1 \end{bmatrix} & y_{12} \cdot \begin{bmatrix} 1 & -1 \\ -1 & 1 \end{bmatrix} \\ y_{21} \cdot \begin{bmatrix} 1 & -1 \\ -1 & 1 \end{bmatrix} & y_{22} \cdot \begin{bmatrix} 1 & -1 \\ -1 & 1 \end{bmatrix} \end{bmatrix} \cdot \begin{bmatrix} v_1 \\ v_2 \\ v_3 \\ v_4 \end{bmatrix} + \begin{bmatrix} j_{\text{S1}} \cdot \begin{bmatrix} 1 \\ -1 \end{bmatrix} \\ j_{\text{S2}} \cdot \begin{bmatrix} 1 \\ -1 \end{bmatrix} \end{bmatrix}. (6)$$

Therefore, once the nodal admittance equation containing the external terminal node of DAB PM is calculated, the short-circuit admittance parameters can be obtained directly.

B. Nodal Admittance Equation of DAB Power Module

A classical DAB PM structure is shown in Fig. 1(b). It is known from [24] that the equivalent modelling of the transformer is the key challenge of DAB PM. First, the model of the transformer in [24] takes one time-step approximation, which may result in some additional errors. Second, the transformer resistances are comparable to the semiconductor switch resistances, which are necessary to be considered to increase the accuracy and expand the application scopes of the model. Hence, an improved transformer model is introduced in this section.

The T-type equivalent circuit of the transformer in Fig. 1(b) is shown in Fig. 5(a).
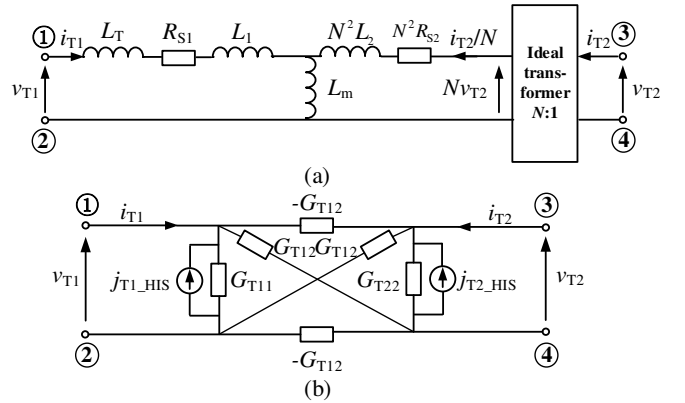

Fig. 5. The transformer models. (a) T-type equivalent circuit; (b) Discretized model using TR integration method.

The inductances include the auxiliary inductance L_T, the primary-side leakage reactance L_1, the excitation reactance L_m and the secondary-side leakage reactance L_2. They have been

referred to the primary side of the transformer [16]. R_{S1} and R_{S2} are the primary and secondary winding resistances. Moreover, the ideal transformer is used between the primary and secondary sides, so that the port voltages (v_{T1}, v_{T2}) and currents (i_{T1}, i_{T2}) are electrically isolated as the actual transformer. The discretized model of the transformer using the trapezoidal rule (TR) is proposed, as shown in Fig. 5(b), where the subscript "T1" represents the primary side and "T2" represents the secondary side.

The KVL of the T-type equivalent circuit in Fig. 5(a) is written as

$$\begin{bmatrix} v_{T1}(t) \\ v_{T2}(t) \end{bmatrix} = \begin{bmatrix} L_T + L_1 + L_m & L_m / N \\ L_m / N & L_2 + L_m / N^2 \end{bmatrix} \cdot \begin{bmatrix} \dfrac{di_{T1}(t)}{dt} \\ \dfrac{di_{T2}(t)}{dt} \end{bmatrix}. \quad (7)$$

$$+ \begin{bmatrix} R_{S1} & 0 \\ 0 & R_{S2} \end{bmatrix} \cdot \begin{bmatrix} i_{T1}(t) \\ i_{T2}(t) \end{bmatrix}$$

Define

$$\begin{cases} Y_T = \dfrac{\Delta t}{2} \cdot \begin{bmatrix} L_T + L_1 + L_m & L_m / N \\ L_m / N & L_2 + L_m / N^2 \end{bmatrix}^{-1} \\ R = \begin{bmatrix} R_{S1} & 0 \\ 0 & R_{S2} \end{bmatrix}, \quad I = \begin{bmatrix} 1 & 0 \\ 0 & 1 \end{bmatrix} \end{cases}. \quad (8)$$

Discretize (7) with the TR integration method, then

$$\begin{bmatrix} i_{T1}(t) \\ i_{T2}(t) \end{bmatrix} = G_T \cdot \begin{bmatrix} v_{T1}(t) \\ v_{T2}(t) \end{bmatrix} - \begin{bmatrix} j_{T1\_HIS}(t) \\ j_{T2\_HIS}(t) \end{bmatrix}. \quad (9)$$

The expression of G_T is given in (10), where G_{T11} and G_{T22} both represent the self-admittance, G_{T12} and $-G_{T12}$ represent the mutual-admittance, and K is a coefficient matrix. These parameters will be constants once the step size, integration method and parameters of the transformer are determined [16]. j_{T1_HIS} and j_{T2_HIS} represent the history current sources, which can be obtained before the EMT calculation of each time-step.

$$\begin{cases} G_T = [I + Y_T \cdot R]^{-1} \cdot Y_T = [Y_T^{-1} + R]^{-1} = \begin{bmatrix} G_{T11} & G_{T12} \\ G_{T12} & G_{T22} \end{bmatrix} \\ K = [I + Y_T \cdot R]^{-1} [I - Y_T \cdot R] \\ \begin{bmatrix} j_{T1\_HIS}(t) \\ j_{T2\_HIS}(t) \end{bmatrix} = -G_T \cdot \begin{bmatrix} v_{T1}(t - \Delta t) \\ v_{T2}(t - \Delta t) \end{bmatrix} - K \cdot \begin{bmatrix} i_{T1}(t - \Delta t) \\ i_{T2}(t - \Delta t) \end{bmatrix} \end{cases}. \quad (10)$$

After that, the companion circuit of DAB PM can be obtained as shown in Fig. 6. In which, the switches are represented by on-state conductance G_{ON} and off-state conductance

G_{OFF} [27], and the internal capacitors are discretized to Norton equivalent circuit ($G_C//j_{C\_HIS}$) based on the Dommel's method [28]. The simplification may lead to inapplicability when simulating the device-level behaviors, but it is enough for simulating the module-level dynamics [29].
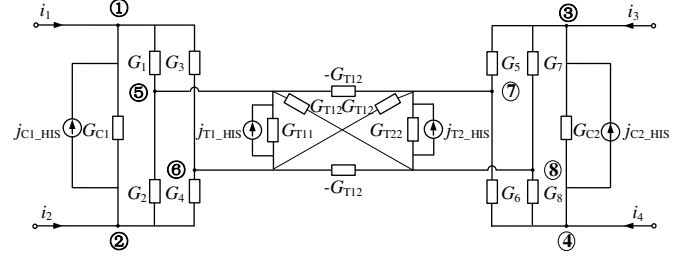

Fig. 6. Companion circuit of DAB PM.

Using the idea of partitioned matrix separating the internal and external nodes, the nodal admittance equation of DAB PM is written as in (11), which can be simply expressed as

$$\begin{bmatrix} A & B \\ B^T & C \end{bmatrix} \cdot \begin{bmatrix} v_{EX} \\ v_{IN} \end{bmatrix} = \begin{bmatrix} j_{EX} \\ j_{IN} \end{bmatrix} + \begin{bmatrix} i_{EX} \\ 0 \end{bmatrix}, \quad (12)$$

where A, B and C are 4×4 sized partitioned matrices, the subscript "EX" represents the external nodes, "IN" represents the internal nodes.

C. Preprocessing of Nodal Admittance Equation

Referring to [19] and [20], the internal nodes can be eliminated by (13) to obtain the equivalent circuit only containing the external terminals.

$$\begin{cases} i_{EX} = Y_{EX} v_{EX} + j_S \\ Y_{EX} = A - B \cdot C^{-1} \cdot B^T \\ j_S = B \cdot C^{-1} \cdot j_{IN} - j_{EX} \end{cases}, \quad (13)$$

where Y_{EX} and j_S represent the equivalent nodal admittance matrix and equivalent historical current sources. After that, (14) is used to update the internal information.

$$v_{IN} = C^{-1} \cdot (j_{IN} - B^T \cdot v_{EX}). \quad (14)$$

It is observed that the nodal admittance matrix in (12) has high sparsity, hence, (15) is obtained by dividing A, B and C into four 2×2 sized partitioned matrices, respectively.

$$A = \left[\begin{array}{c|c} A_{11} & 0 \\ \hline 0 & A_{22} \end{array}\right], B = \left[\begin{array}{c|c} B_{11} & 0 \\ \hline 0 & B_{22} \end{array}\right], C = \left[\begin{array}{c|c} C_{11} & C_{12} \\ \hline C_{12} & C_{22} \end{array}\right]. \quad (15)$$

For more convenient representations, C^{-1} in (13) and (14) is rewritten as 4×4 sized matrix Q, which is also divided into four 2×2 partitioned matrices as (16).

$$\left[\begin{array}{cccc:cccc} G_{C1}+G_1+G_3 & -G_{C1} & 0 & 0 & -G_1 & -G_3 & 0 & 0 \\ -G_{C1} & G_{C1}+G_2+G_4 & 0 & 0 & -G_2 & -G_4 & 0 & 0 \\ 0 & 0 & G_{C2}+G_5+G_7 & -G_{C2} & 0 & 0 & -G_5 & -G_7 \\ 0 & 0 & -G_{C2} & G_{C2}+G_6+G_8 & 0 & 0 & -G_6 & -G_8 \\ \hdashline -G_1 & -G_2 & 0 & 0 & G_{T11}+G_1+G_2 & -G_{T11} & G_{T12} & -G_{T12} \\ -G_3 & -G_4 & 0 & 0 & -G_{T11} & G_{T11}+G_3+G_4 & -G_{T12} & G_{T12} \\ 0 & 0 & -G_5 & -G_6 & G_{T12} & -G_{T12} & G_{T22}+G_5+G_6 & -G_{T22} \\ 0 & 0 & -G_7 & -G_8 & -G_{T12} & G_{T12} & -G_{T22} & G_{T22}+G_7+G_8 \end{array}\right] \cdot \begin{bmatrix} v_1 \\ v_2 \\ v_3 \\ v_4 \\ v_5 \\ v_6 \\ v_7 \\ v_8 \end{bmatrix} = \begin{bmatrix} j_{C1\_HIS} \\ -j_{C1\_HIS} \\ j_{C2\_HIS} \\ -j_{C\_HIS} \\ j_{T1\_HIS} \\ -j_{T1\_HIS} \\ j_{T2\_HIS} \\ -j_{T2\_HIS} \end{bmatrix} + \begin{bmatrix} i_1 \\ i_2 \\ i_3 \\ i_4 \\ 0 \\ 0 \\ 0 \\ 0 \end{bmatrix} \quad (11)$$

$$Q = \begin{bmatrix} Q_{11} & \vdots & Q_{12} \\ \hdashline Q_{12}^T & \vdots & Q_{22} \end{bmatrix}$$

$$= \begin{bmatrix} C_{11}^{-1} + C_{11}^{-1} \cdot C_{12} \cdot M_{22}^{-1} \cdot C_{12} \cdot C_{11}^{-1} & \vdots & -C_{11}^{-1} \cdot C_{12} \cdot M_{22}^{-1} \\ \hdashline -M_{22}^{-1} \cdot C_{12} \cdot C_{11}^{-1} & \vdots & M_{22}^{-1} \end{bmatrix}, (16)$$

where

$$M_{22} = C_{22} - C_{12} \cdot C_{11}^{-1} \cdot C_{12}. \qquad (17)$$

According to (15)-(17), Y_{EX} and j_S in (13) are reorganized as

$$\begin{cases} Y_{EX} = \begin{bmatrix} A_{11} - B_{11} \cdot Q_{11} \cdot B_{11}^T & \vdots & -B_{11} \cdot Q_{12} \cdot B_{22}^T \\ \hdashline -B_{22} \cdot Q_{12}^T \cdot B_{11}^T & \vdots & A_{22} - B_{22} \cdot Q_{22} \cdot B_{22}^T \end{bmatrix} \\ j_S = \begin{bmatrix} B_{11} \cdot Q_{11} & B_{11} \cdot Q_{12} \\ B_{22} \cdot Q_{12} & B_{22} \cdot Q_{22} \end{bmatrix} \cdot j_{IN} - j_{EX} \end{cases}. \quad (18)$$

In addition, under the non-blocking mode, the four IGBTs in the H-bridge will be in two switching pairs to prevent the short-circuit of the capacitor, hence

$$G_1 + G_2 = G_3 + G_4 = G_5 + G_6 = G_7 + G_8 = G_{ON} + G_{OFF}. \quad (19)$$

Define $G_X \triangleq G_{ON} + G_{OFF}$. Then G_X, G_{T11}, G_{T12} and G_{T22} in (10) are constants. Hence, it can be observed that C is a symmetric constant matrix regardless of the switching pulses, which indicates that Q is also a symmetric constant matrix. Combine (16), (17) and (19), Q can be simplified as (20).

$$Q = \begin{bmatrix} \begin{bmatrix} q_1 & q_2 \\ q_2 & q_1 \end{bmatrix} & \vdots & q_3 \cdot \begin{bmatrix} 1 & -1 \\ -1 & 1 \end{bmatrix} \\ \hdashline q_3 \cdot \begin{bmatrix} 1 & -1 \\ -1 & 1 \end{bmatrix} & \vdots & \begin{bmatrix} q_4 & q_5 \\ q_5 & q_4 \end{bmatrix} \end{bmatrix}, \quad (20)$$

where q_1-q_5 are constant parameters as given in (21).

$$\begin{cases} q_1 = \dfrac{1}{2 \times G_X} + \dfrac{2G_{T22} + G_X}{2 \times [(2G_{T22} + G_X) \times (2G_{T11} + G_X) - 4G_{T12} \times G_{T12}]} \\ q_2 = \dfrac{1}{2 \times G_X} - \dfrac{2G_{T22} + G_X}{2 \times [(2G_{T22} + G_X) \times (2G_{T11} + G_X) - 4G_{T12} \times G_{T12}]} \\ q_3 = \dfrac{-G_{T12}}{(2G_{T22} + G_X) \times (2G_{T11} + G_X) - 2G_{T12} \times 2G_{T12}} \\ q_4 = \dfrac{(2G_{T11} + G_X) \times (G_{T22} + G_X) - 2G_{T12} \times G_{T12}}{G_X \times [(2G_{T22} + G_X) \times (2G_{T11} + G_X) - 4G_{T12} \times G_{T12}]} \\ q_5 = \dfrac{(2G_{T11} + G_X) \times G_{T22} - 2G_{T12} \times G_{T12}}{G_X \times [(2G_{T22} + G_X) \times (2G_{T11} + G_X) - 4G_{T12} \times G_{T12}]} \end{cases}. (21)$$

Moreover, Y_{EX} and j_S in (18) are preprocessed based on (19) to (21), as

$$Y_{EX} = \begin{bmatrix} y_{11} \cdot \begin{bmatrix} 1 & -1 \\ -1 & 1 \end{bmatrix} & \vdots & y_{12} \cdot \begin{bmatrix} 1 & -1 \\ -1 & 1 \end{bmatrix} \\ \hdashline y_{12} \cdot \begin{bmatrix} 1 & -1 \\ -1 & 1 \end{bmatrix} & \vdots & y_{22} \cdot \begin{bmatrix} 1 & -1 \\ -1 & 1 \end{bmatrix} \end{bmatrix}; \quad j_S = \begin{bmatrix} j_{S1} \cdot \begin{bmatrix} 1 \\ -1 \end{bmatrix} \\ j_{S2} \cdot \begin{bmatrix} 1 \\ -1 \end{bmatrix} \end{bmatrix}, (22)$$

wherein the values of y_{11}, y_{12}, y_{22}, j_{S1} and j_{S2} can be directly calculated using (23).

The variables K_1-K_5 are controlled by the firing pulses of IGBTs T_1-T_8, as shown in (24). Other parameters related to q_1-q_5, G_{ON} and G_{OFF} are constants, which need to be calculated only once at the beginning of the simulation.

$$\begin{cases} y_{11} = G_{C1} + (q_1 + q_2) \cdot 2 \cdot G_{ON} \cdot G_{OFF} \\ \qquad + K_1 \cdot q_2 \cdot (G_{ON} - G_{OFF})^2 \\ y_{12} = -K_2 \cdot q_3 \cdot (G_{ON} - G_{OFF})^2 \\ y_{22} = G_{C2} + (q_4 + q_5) \cdot 2 \cdot G_{ON} \cdot G_{OFF} \\ \qquad + K_3 \cdot q_5 \cdot (G_{ON} - G_{OFF})^2 \\ j_{S1} = K_4 \cdot (q_1 - q_2) \cdot (G_{OFF} - G_{ON}) \cdot j_{T1\_HIS} \\ \qquad + K_4 \cdot q_3 \cdot 2 \cdot (G_{OFF} - G_{ON}) \cdot j_{T2\_HIS} - j_{C1\_HIS} \\ j_{S2} = K_5 \cdot (q_4 - q_5) \cdot (G_{OFF} - G_{ON}) \cdot j_{T2\_HIS} \\ \qquad + K_5 \cdot q_3 \cdot 2 \cdot (G_{OFF} - G_{ON}) \cdot j_{T1\_HIS} - j_{C2\_HIS} \end{cases}. \quad (23)$$

$$\begin{cases} K_1 = \begin{cases} 1, T_1 = T_4 \\ 0, T_1 = T_3 \end{cases}; \quad K_3 = \begin{cases} 1, T_5 = T_8 \\ 0, T_5 = T_7 \end{cases} \\ K_2 = \begin{cases} 0, T_1 = T_3 \ \text{ or } \ T_5 = T_7 \\ 1, T_1 = T_5 \ \text{ and } \ (T_1 = T_4, T_5 = T_8) \\ -1, T_1 \neq T_5 \ \text{ and } \ (T_1 = T_4, T_5 = T_8) \end{cases} \\ K_4 = \begin{cases} 1, T_1 = T_4 = 1 \\ 0, T_1 = T_3 \\ -1, T_1 = T_4 = 0 \end{cases}; \quad K_5 = \begin{cases} 1, T_5 = T_8 = 1 \\ 0, T_5 = T_7 \\ -1, T_5 = T_8 = 0 \end{cases} \end{cases}. \quad (24)$$

Equation (22) has the same form as (6), hence the equivalent circuit of DAB PM is the same as Fig. 3. Meanwhile, DAB PM is a reciprocal two-port since Y_{EX} is symmetric.

Moreover, the transformer terminal voltages v_5 to v_8 in (11) will not directly affect the equivalent modelling of the PMs. They are reflected in the port voltages v_{T1} and v_{T2} in (10). Hence, the reverse of the internal information in (14) can be transformed into the calculation of new values of v_{T1} and v_{T2}. Using the same idea of preprocessing and substituting (20) to (22), the reverse process in (14) can also be simplified as

$$\begin{cases} v_{T1} = 2 \cdot (q_2 - q_1) \cdot j_{T1\_HIS} - 4 \cdot q_3 \cdot j_{T2\_HIS} - \\ \qquad (G_{OFF} - G_{ON}) \cdot [K_4 \cdot (q_1 - q_2) \cdot v_{IN} + 2 \cdot K_5 \cdot q_3 \cdot v_{OUT}] \\ v_{T2} = 2 \cdot (q_5 - q_4) \cdot j_{T2\_HIS} - 4 \cdot q_3 \cdot j_{T1\_HIS} - \\ \qquad (G_{OFF} - G_{ON}) \cdot [K_5 \cdot (q_4 - q_5) \cdot v_{OUT} + 2 \cdot K_4 \cdot q_3 \cdot v_{IN}] \end{cases}, (25)$$

where v_{IN} and v_{OUT} are the new port voltages of DAB PMs obtained from the EMT solver and equation (1), and K_4 and K_5 are controlled by (24).

IV. ANALYSIS OF APPLICABILITY

A. Applicability Considering Transformer Saturation

In Fig. 5, the transformer saturation is ignored to simplify the model without sacrificing its accuracy and applicability. To improve the performance of the equivalent model in more conditions, the transformer saturation is discussed in this section.

Reference [30] presents a T-type equivalent model considering transformer saturation. As shown in Fig. 7(a), the magnetizing current is divided into two components: the compensating current source i_m and the current in the linear inductance L_m. Particularly, with strict mathematical derivation, reference [30] further divides the saturation current into terminal current sources i_{m1} and i_{m2}, as shown in Fig. 7(b).
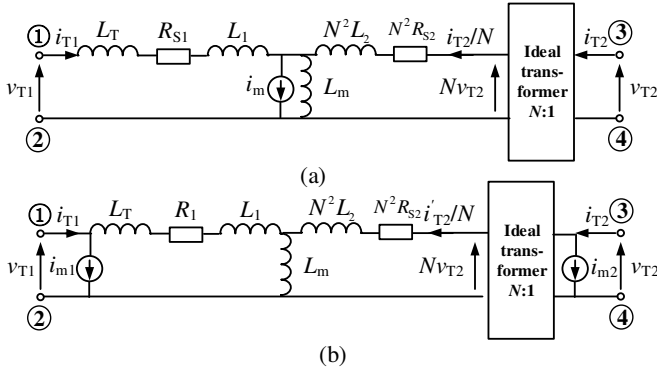
Fig. 7. The transformer models considering saturation. (a) T-type equivalent circuit; (b) Mathematical equivalent model.

Fig. 8. Equivalent circuit of CHB PM. (a) Structure; (b) Companion circuit; (c) Equivalent circuit.

Based on the equivalent model in Fig. 7(b), the KVL in (7) is rewritten as

$$\begin{bmatrix} v_{T1}(t) \\ v_{T2}(t) \end{bmatrix} = \begin{bmatrix} L_T + L_1 + L_m & L_m / N \\ L_m / N & L_2 + L_m / N^2 \end{bmatrix} \cdot \begin{bmatrix} \dfrac{d[i_{T1}(t) - i_{m1}(t)]}{dt} \\ \dfrac{d[i_{T2}(t) - i_{m2}(t)]}{dt} \end{bmatrix}$$
$$+ \begin{bmatrix} R_1 & 0 \\ 0 & R_2 \end{bmatrix} \cdot \begin{bmatrix} i_{T1}(t) - i_{m1}(t) \\ i_{T2}(t) - i_{m2}(t) \end{bmatrix}. \quad (26)$$

It can be observed that the discretized expression and equivalent circuit of the transformer can be determined once i_{m1} and i_{m2} are obtained, as shown in (27) and (28).

$$\begin{bmatrix} i_{T1}(t) \\ i_{T2}(t) \end{bmatrix} = \boldsymbol{G}_T \cdot \begin{bmatrix} v_{T1}(t) \\ v_{T2}(t) \end{bmatrix} - \begin{bmatrix} j^*_{T1\_HIS}(t) \\ j^*_{T2\_HIS}(t) \end{bmatrix}, \quad (27)$$

$$\begin{bmatrix} j^*_{T1\_HIS}(t) \\ j^*_{T2\_HIS}(t) \end{bmatrix} = -\boldsymbol{G}_T \cdot \begin{bmatrix} v_{T1}(t-\Delta t) \\ v_{T2}(t-\Delta t) \end{bmatrix} - \boldsymbol{K} \cdot \begin{bmatrix} i_{T1}(t-\Delta t) \\ i_{T2}(t-\Delta t) \end{bmatrix}$$
$$+ \boldsymbol{K} \cdot \begin{bmatrix} i_{m1}(t-\Delta t) \\ i_{m2}(t-\Delta t) \end{bmatrix} - \begin{bmatrix} i_{m1}(t) \\ i_{m2}(t) \end{bmatrix}, \quad (28)$$

where $\boldsymbol{G}_T$ and $\boldsymbol{K}$ can be obtained from (10). Since equations (27) and (9) have the same expression, the transformer equivalent circuits are identical as well. Therefore, considering the transformer saturation in the proposed equivalent model will not bring too much additional preprocessing burden and thereby, will not limit its applicability.

B. Applicability to CHB and MAB PMs

Due to the isolation transformers, the port characteristics represented in (5) are also applicable for other types of SST PMs, such as CHB, and MAB. The degree of freedom of the nodes in such PMs is usually 2 or 3, resulting in a high sparsity of the node admittance matrix. Therefore, it is easy to apply the preprocessing method of the nodal admittance equation in Section III to other SST PMs.

Taking CHB as an example, its PM structure is shown in Fig. 8(a). Based on the equivalent circuit of DAB PM in Fig. 3, the companion circuit of the CHB can be directly simplified as the circuit in Fig. 8(b), where G_{H1} to G_{H4} are the on-state or off-state of the four switches in the input H-bridge.
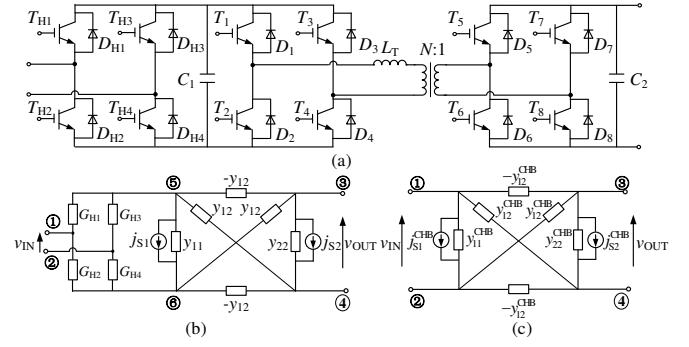
Similar to (11), the nodal admittance equation of CHB is

$$\begin{bmatrix} G_{H1}+G_{H2} & 0 & 0 & 0 & -G_{H1} & -G_{H2} \\ 0 & G_{H3}+G_{H4} & 0 & 0 & -G_{H3} & -G_{H4} \\ 0 & 0 & y_{22} & -y_{22} & y_{12} & -y_{12} \\ 0 & 0 & -y_{22} & y_{22} & -y_{12} & y_{12} \\ -G_{H1} & -G_{H3} & y_{12} & -y_{12} & y_{11}+G_{H1}+G_{H3} & -y_{11} \\ -G_{H2} & -G_{H4} & -y_{12} & y_{12} & -y_{11} & y_{11}+G_{H2}+G_{H4} \end{bmatrix} . \quad (29)$$
$$\cdot \begin{bmatrix} v_1 \\ v_2 \\ v_3 \\ v_4 \\ v_5 \\ v_6 \end{bmatrix} = \begin{bmatrix} i_1 \\ i_2 \\ i_3 \\ i_4 \\ 0 \\ 0 \end{bmatrix} + \begin{bmatrix} 0 \\ 0 \\ -j_{S2} \\ j_{S2} \\ -j_{S1} \\ j_{S1} \end{bmatrix}$$

It can be seen that the nodal admittance matrix exhibits a high sparsity and symmetry. Therefore, the short-circuit admittance equation of CHB PM can be obtained by performing the same preprocessing process as (15)-(24), which is given in (30).

$$\begin{bmatrix} i_{IN} \\ i_{OUT} \end{bmatrix} = \begin{bmatrix} y_{11}^{CHB} & y_{12}^{CHB} \\ y_{12}^{CHB} & y_{22}^{CHB} \end{bmatrix} \cdot \begin{bmatrix} v_{IN} \\ v_{OUT} \end{bmatrix} + \begin{bmatrix} j_{S1}^{CHB} \\ j_{S2}^{CHB} \end{bmatrix}, \quad (30)$$

where y_{11}^{CHB}, y_{12}^{CHB}, y_{22}^{CHB} and j_{S1}^{CHB}, j_{S2}^{CHB} can be calculated using (31).

$$\begin{cases} y_{11}^{CHB} = \left[y_{11} \cdot (G_{ON}+G_{OFF})^2 + 2 \cdot G_{ON} \cdot G_{OFF} \cdot (G_{ON}+G_{OFF}) \right] / \Delta \\ y_{12}^{CHB} = \left[K_6 \cdot y_{12} \cdot (G_{ON}^2 - G_{OFF}^2) \right] / \Delta \\ y_{22}^{CHB} = y_{22} - \left[2 \cdot y_{12}^2 \cdot (G_{ON}+G_{OFF}) \right] / \Delta \\ j_{S1}^{CHB} = \left[K_6 \cdot j_{S1} \cdot (G_{ON}^2 - G_{OFF}^2) \right] / \Delta \\ j_{S2}^{CHB} = j_{S2} - \left[2 \cdot j_{S1} \cdot y_{12} \cdot (G_{ON}+G_{OFF}) \right] / \Delta \\ \Delta = 2 \cdot y_{11} \cdot (G_{ON}+G_{OFF}) + K_7 \cdot (G_{ON}+G_{OFF})^2 + \\ \quad (1-K_7) \cdot 4 \cdot G_{ON} \cdot G_{OFF} \end{cases} \quad (31)$$

Compared with DAB PM, there are two new variables K_6 and K_7 in (31) for CHB PM, which are controlled by the firing pulses of T_{H1}-T_{H4} shown in (32). The equivalent circuit of CHB PM is illustrated in Fig. 7(c).

$$K_6 = \begin{cases} 1, T_{H1} = T_{H4} = 1 \\ 0, T_{H1} = T_{H3} \\ -1, T_{H1} = T_{H4} = 0 \end{cases} ; \quad K_7 = \begin{cases} 1, T_{H1} = T_{H4} \\ 0, T_{H1} = T_{H3} \end{cases}. \quad (32)$$

It is noted that both DAB and CHB are two-port PMs, which means that their short-circuit admittance parameter matrices are second order. But for MAB, the order of the matrix will increase with the number of PM ports.

C. Applicability to SAB and Resonant Converters

Besides DAB, CHB and MAB PMs, the SST can be made of SAB and various types of resonant converters. Taking the LLC resonant converter shown in Fig. 9 as an example, it contains a resonant unit consists of the series resonance inductance L_S, parallel resonance inductance L_P and series resonance capacitance C_S.
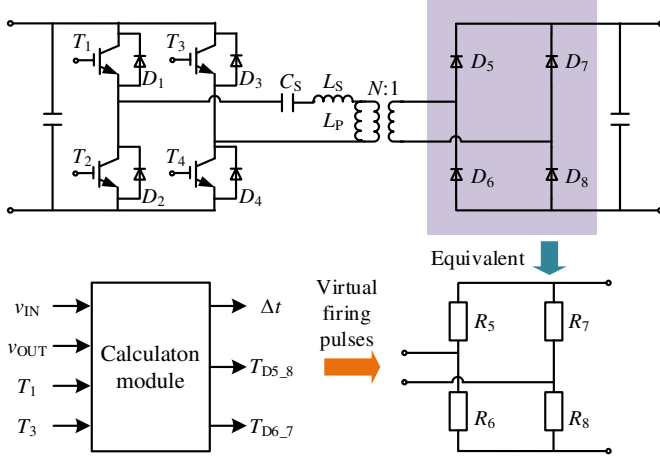

Fig. 9. Equivalent process of the LLC resonance converters.

Compared with the fully controlled PMs, there are two main difficulties when developing the equivalent circuit containing stand-alone diodes. First, the on-off states of these diodes are determined by the device currents and voltages. Therefore, the previous equivalent modelling method cannot be used directly. Second, in software with fixed time-step simulation such as PSCAD/EMTDC, the diode switching process may occur between two time-steps. It may lead to additional errors and instability due to the lack of interpolation.

To improve the performance of the proposed model, an improved simulation solution of the LLC resonant converter is proposed as follows:

Step 1: Generate the virtual firing pulses of diodes. According to [21], the mathematical model of the LLC resonant converter can be obtained. Then, the switching time of the diodes will be predicted by a calculation module, as shown in Fig. 9. Therefore, the uncontrolled diodes are modelled as on-state or off-state resistances controlled by the virtual firing pulses T_{D5_8} and T_{D6_7}.

Step 2: Obtain the equivalent circuit of the PM. Using the proposed modelling method in Sections II and III, the equivalent parameters can be calculated.

Step 3: Simulate using variable time-steps. Through the calculation in Step 1, the suitable time-step Δt will be selected considering both the simulation accuracy and switching time.

It should be mentioned that the calculation in Step 1 requires a high-order integration algorithm to meet the accuracy requirements, which will bring a lot of calculations and slow down the simulation speed. Then, the existence of L_S, L_P and C_S will increase the difficulty of the preprocessing process in Step 2.

V. SIMULATION VERIFICATION

In this section, the accuracy and efficiency of the proposed

equivalent MMC-based SST model (EM1) is verified by the comparisons with the detailed model (DM) and the developed equivalent model (EM2) using the existing equivalent modelling algorithm in [24]. The Thevenin equivalent model of the MMC mentioned in [31] is used in the simulation.

All simulations are performed on a computer with a 1.80 GHz AMD A8-7100 Radeon R5, 8 Compute Cores 4C+4G CPU and PSCAD/EMTDC Professional V4.6. The simulation time-step is set as 5 μs.

A. Configuration and Control Strategy of the Test System

The schematic diagram of the test SST system is shown in Fig. 10, which is composed of MMC, HFL based on DAB PMs, a photovoltaic (PV) station and a DC resistive load. Parameters are given in TABLE II.
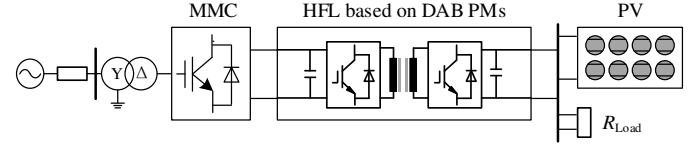

Fig. 10. MMC-based SST test system.

TABLE II
SYSTEM PARAMETERS OF THE MMC-BASED SST

Symbols	Items	Values
N_{SM}	Number of SMs in MMC	10
C_{SM}	MMC SM capacitance	10 mF
V_{ac}	Voltage of the AC source	10 kV
V_H	Rated voltage of the MV DC bus	16 kV
V_L	Rated voltage of the LV DC bus	1.5 kV
N_{DAB}	Number of DAB PMs	10
S_{tr}	Rated capacity of transformer	0.25 MVA
L_{tr}	Stray inductance of the transformer	100 μH
k	Transformer ratio	1
C_{IN}	Capacitance of input-side of DAB	1 mF
C_{OUT}	Capacitance of output-side of DAB	2 mF
R_{Load}	DC load	3 Ω

The control mode including the outer voltage loop and inner current loop is used in the MMC to regulate the MVDC bus voltage. There is a Boost circuit at the terminal of the photovoltaic station to manage its output power. Moreover, the single-phase shift (SPS) control is applied to balance the DAB's output DC voltage [32].

B. Accuracy Test

Typically, the switching frequency of the IGBTs and transformers ranges from 1 kHz to 20 kHz, which requires a simulation time-step between 1 μs and 10 μs [15]. The increase of the frequency will decrease the control accuracy and further increase the truncation error of different integration methods. In addition, compared to EM1, EM2 contains a single time-step approximation, whose accuracy is more sensitive to the increase of the frequency. Therefore, two different frequencies, i.e., 1 kHz and 10 kHz are set to verify the accuracy in comparing DM, EM1, and EM2.

Different working conditions are set to test the simulation accuracy: a) before $t = 3.5$ s, MMC is charged and HFL remains blocked; b) at $t = 3.5$ s, HFL is de-blocked and enters the start-up process; c) at $t = 4$ s, the SST system reaches the
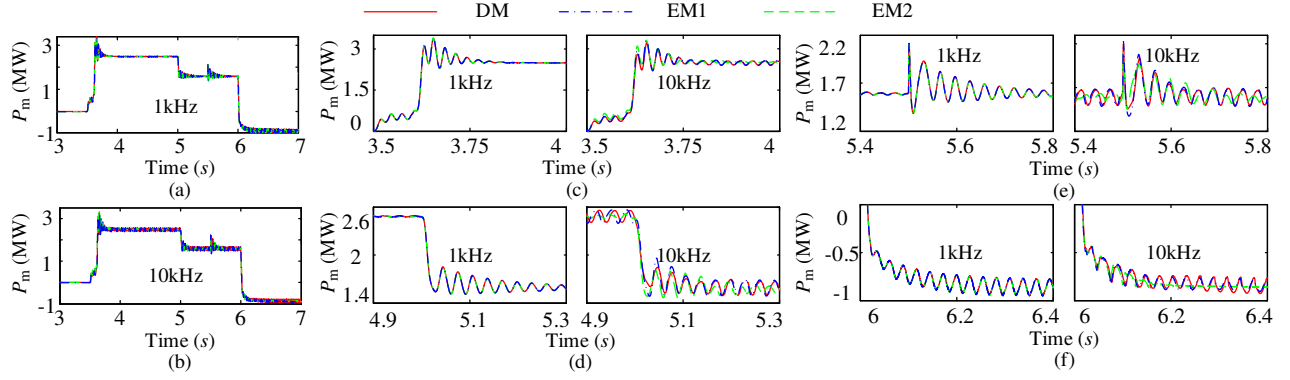
Fig. 11. Behavior of the power. (a) The whole process (1 kHz); (b) The whole process (10 kHz); The zoomed-in views: (c) Start-up; (d) Voltage change; (e) Fault and recovery; (f) Power reversal.

steady state; d) at $t = 5$ s, DAB's output voltage is changed to 0.8 p.u.; e) at $t = 5.5$ s, an LVDC side pole-to-pole short-circuit with a fault resistance 0.1 Ω occurs and is cleared after 0.003 s; f) at $t = 6$ s, the photovoltaic station is deployed to replace the DC resistance, and the power is reversed.

The power under 1 kHz and 10 kHz is shown in Fig. 11. Figs. 11(a) and 11(b) show the whole process. Four different states including the start-up, voltage change, fault and recovery and power reversal are illustrated in Figs. 11(c)-(f). The average values of the maximum relative errors (AMEs) of the four states under different switching frequencies are given in Table III.

TABLE III
THE AVERAGE VALUES OF MAXIMUM RELATIVE ERRORS

Frequency (kHz)	EM1 (%)	EM2 (%)
1	1.84	2.14
10	6.54	12.7

Under low frequency as 1 kHz, EM1 and EM2 show similar high accuracy with the AME below 2.2%. The AMEs of the two EMs increase with the frequency, and the AME of EM2 rises faster than EM1. When the frequency reaches 10 kHz, the AME of EM2 exceeds 12%, while the proposed EM1 still maintain a low level less than 6.6%. It means that EM1 is more suitable for the equivalent simulation of complex coupled SST systems.

C. Computation Efficiency Test

In this section, the models of independent open-loop HFL based on the DM, EM1 and EM2 are tested. In these models, the input-side of the converter is represented by a DC voltage source, and a fixed phase-shift ratio is used in the controller.
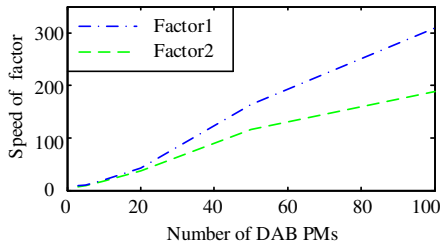

Fig. 12. Comparison of speedup capability.

The simulation duration and the frequency are set as 5 s and 1 kHz, respectively. The computation time, as well as the speedup factors of EM1 and EM2 varying with the number of DAB PMs are listed in Table IV, and the results are also depicted in Fig. 12.

TABLE IV
COMPUTATION TIME OF DC/DC CONVERTER

No.	DM (s)	EM1 (s)	Factor1	EM2 (s)	Factor2
3	56.27	6.36	8.84	7.47	7.53
5	86.53	8.24	10.50	9.19	9.42
10	253.56	12.82	19.78	14.41	17.59
20	919.08	21.60	42.55	24.89	36.93
50	6774.18	41.40	163.63	58.59	115.62
100	23080.35	74.51	309.76	122.77	187.99

With the increasing number of DAB PMs, the computation times of DM increase exponentially while EM1 and EM2 increase linearly. When the DAB number reaches 50, the speedup of EM1 is over 2 orders of magnitude faster than the DM, and is also 1.5 times faster than EM2.

The whole closed-loop MMC based SST system is also tested. The results are given in Table V. The parameters of the system are the same as Section IV.B and the frequency range from 1 kHz to 10 kHz. The results show that the computation time of the EM1 does not change with frequency, but the computation time of the DM increases significantly. Although there is an MMC and the control system reduces the speedup factor of EM1 comparing with the independent HFL, the factors of EM1 still maintain at a higher level over 10.

TABLE V
COMPUTATION TIME OF MMC-BASED SST

Frequency (kHz)	DM (s)	EM1 (s)	Factor1	EM2 (s)	Factor2
1	1399.67	201.24	6.96	214.91	6.51
5	2246.52	200.76	11.19	210.23	10.68
10	2880.13	202.22	14.24	211.55	13.61

D. Benefits of the Proposed Model

Compared with the existing models of the SSTs mentioned in the Introduction, especially the decoupled equivalent model in [24], the proposed EMT equivalent model has the following advantages:

1) Using the conversion of the port equation parameters in Section II and the preprocessing of the nodal admittance equation in Section III, the SST equivalent circuits can be directly obtained through simple multiplication and addition of the

constants in (2) and (23). It avoids the multiplication and inversion of high-order matrices and therefore, effectively accelerates the calculation speed;

2) The equivalent modelling process does not involve approximations. It achieves a high accuracy under different conditions compared with the detailed model. Moreover, the internal information can be accurately updated using (1) and (25) once the external information is obtained;

3) The accelerated modelling method is applicable to other types of SST PMs and connection configurations, even considering the transformer saturation;

4) The modelling method has good parallelism and can easily realize multi-threaded parallel simulation and real-time simulation.

It should be mentioned that the above benefits are achieved by conducting the formula derivation and code programming in advance. However, as long as the converter topology is determined, these tasks only need to be performed once.

VI. EXPERIMENTAL VALIDATION

To validate the proposed accelerated equivalent modelling method, a scale-down SST system in [33] is used to compare with the simulation results.
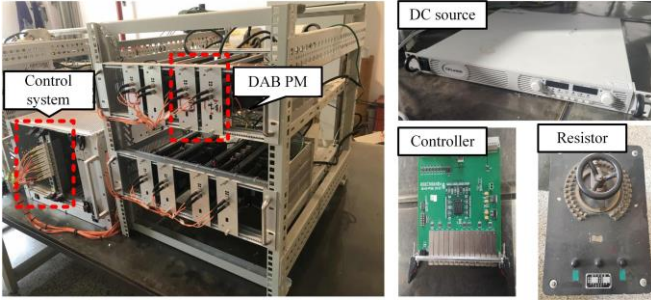

Fig. 13. Experimental platform setup.

Fig. 13 presents the setup of the experimental platform. The parameters are given in Table VI. The SST system consists of a 150 V DC source, four DAB PMs (one of them is used as a redundant module), a control system, and a variable load re-

sistor. The corresponding equivalent models of EM1 and EM2 are also developed in PSCAD/EMTDC using the same parameters.

TABLE VI
PARAMETERS OF THE SST EXPERIMENTAL PLATFORM

Symbols	Items	Values
N_{DAB}	Number of DAB PMs	3
V_{H}	Input DC voltage	150 V
V_{L}	Output DC voltage	50 V
f_{S}	Switching frequency	5 kHz
k	Transformer ratio	1
C_{IN}	Capacitance of input-side of DAB	6.56 mF
C_{OUT}	Capacitance of output-side of DAB	6.56 mF
L_{tr}	Stray inductance of the transformer	62.5 μH
R_{s1}	Primary winding resistance	0.1 Ω
R_{s2}	Secondary winding resistance	0.1 Ω

The control system is built on the PowerPC P2020 + FPGA_6SL X45 and adopts the SPS method to keep the output voltage at 50 V. The power stepped up from 0 to 400 W first and then to 800 W, then stepped down from 800 W to 400 W and then to 0 by switching the load resistor.

Fig. 14 and Table VII provide the simulation and experiment results of EM1 and EM2. The external information for the converter, such as the input and output DC voltages v_{H} and v_{L}, output current i_{OUT}, and the internal information in each PMs, such as the high-frequency voltages and currents v_{tr1}, v_{tr2} and i_{tr1} are all included. Noted that, the units of the experimental waveforms are displayed at the bottom of the subplots.

Under different conditions, the simulation waveforms match very well with the experimental results with a relative error less than 4%. The results show that the relative errors of all waveforms of EM1 are smaller than EM2, which is consistent with the theoretical analysis and the simulation results in Section V.B. The results also show that the proposed equivalent model has very high accuracy and can meet the requirement of simulating the internal and external performances of the SST systems.
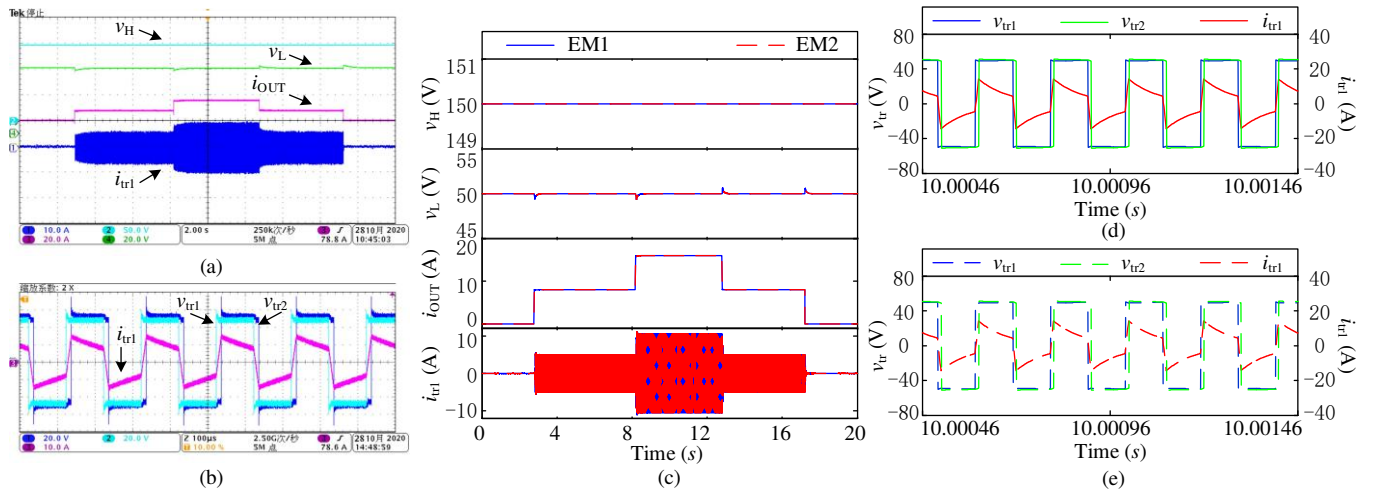

Fig. 14. Waveforms from the simulation and experiment. (a) The whole experiment waveforms; (b) Zoomed-in experiment waveforms; (c) The whole simulation waveforms of EM1 and EM2; (d) Zoomed-in simulation waveforms of EM1; (e) Zoomed-in simulation waveforms of EM2.

VII. CONCLUSIONS

This paper proposes an accelerated EMT equivalent model of MMC-based solid-state transformers (SSTs). The proposed method develops the equivalent circuit of the high-frequency link (HFL) containing only four external terminals by eliminating all internal nodes. Moreover, the port parameters of the HFL are calculated through the preprocessing of the nodal admittance equation and the conversion of short-circuit admittance parameters.

The simulation results show that, with more than 50 PMs, the accelerated equivalent model (EM1) is 2 orders of magnitude faster than the fully detailed model (DM), and is also about 1.5 times more efficient than the equivalent model (EM2) based on the existing algorithms. Under low frequency as 1 kHz, the EM1 and EM2 both show high accuracy with the average value of maximum relative errors (AMEs) below 2.2%. Due to the complex coupling of MMC, the applicability of EM2 will be limited under a higher frequency of 10 kHz. However, the proposed EM1 still maintains the AME at a low level of 6.6%. Moreover, a scale-down SST experimental platform is built to verify the simulation results. The comparisons show that EM1 matches very well with the experimental results with a relative error less than 4%.

In addition, this proposed method is applicable to the equivalent modelling of other SST power modules and connection configurations. Therefore, the proposed accelerated equivalent modelling method is significant for the EMT simulation of SSTs.

REFERENCES

[1] J. E. Huber and J. W. Kolar, "Solid-state transformers: on the origins and evolution of key concepts," *IEEE Ind. Electron. Mag.,* vol. 10, no. 3, pp. 19-28, Sept. 2016.

[2] A. Q. Huang, "Medium-voltage solid-state transformer: technology for a smarter and resilient grid," *IEEE Power Electron. Mag.*, vol. 10, no. 3, pp. 29-42, Sep. 2016.

[3] L. F. Costa, G. Carne, G. Buticchi, et al., "The smart transformer: a solid-state transformer tailored to provide ancillary services to the distribution grid," *IEEE Power Electron. Mag.*, vol. 4, no. 2, pp. 56-67, Jun. 2017.

[4] X. She, A. Q. Huang and R. Burgos, "Review of solid-state transformer technologies and their application in power distribution systems," *IEEE J. Emerg. Sel. Topics Power Electron.*, vol. 1, no. 3, pp. 186-198, Sept. 2013.

[5] J. E. Huber and J. W. Kolar, "Applicability of solid-state transformers in today's and future distribution grids," *IEEE Trans. Smart Grid*, vol. 10, no. 1, pp. 317-326, Jan. 2019.

[6] C. D. Townsend, Y. Yu, G. Konstantinou, et al., "Cascaded H-bridge multilevel PV topology for alleviation of per-phase power imbalances

and reduction of second harmonic voltage ripple," *IEEE Trans. Power Electron.*, vol. 31, no. 8, pp. 5574-5586, Aug. 2016.

[7] T. Liu, X. Yang, W. Chen, et al, "Design and implementation of high efficiency control scheme of dual active bridge based 10 kV/1 MW solid state transformer for PV application," *IEEE Trans. Power Electron.*, vol. 34, no. 5, pp. 4223-4238, May 2019.

[8] B. Zhao, Q. Song, J. Li, et al., "Comparative analysis of multilevel-high-frequency-link and multilevel-DC-link DC–DC transformers based on MMC and dual-active bridge for MVDC application," *IEEE Trans. Power Electron.*, vol. 33, no. 3, pp. 2035-2049, Mar. 2018.

[9] L. F. Costa, F. Hoffmann, G. Buticchi, et al., "Comparative analysis of multiple active bridge converters configurations in modular smart transformer," *IEEE Trans. Ind. Electron.*, vol. 66, no. 1, pp. 191-202, Jan. 2019.

[10] C. Zhao, D. Dujic, A. Mester, et al., "Power electronic traction transformer—medium voltage prototype," *IEEE Trans. Ind. Electron.* vol. 61, no. 7, pp. 3257-3268, Jul. 2014.

[11] L. H. S. C. Barreto, D. de A. Honório, D. de Souza Oliveira, et al., "An interleaved-stage AC–DC modular cascaded multilevel converter as a solution for MV railway applications," *IEEE Trans. Ind. Electron,* vol. 65, no. 4, pp. 3008-3016, Apr. 2018.

[12] A. J. B. Bottion and I. Barbi, "Input-series and output-series connected modular output capacitor full-bridge PWM DC–DC converter," *IEEE Trans. Ind. Electron.*, vol. 62, no. 10, pp. 6213-6221, Oct. 2015.

[13] F. Ruiz, M. A. Perez, J. R. Espinosa, et al., "Surveying solid-state transformer structures and controls: providing highly efficient and controllable power flow in distribution grids," *IEEE Ind. Electron. Mag.*, vol. 14, no. 1, pp. 56-70, Mar. 2020.

[14] F. Gao, Z. Li, P. Wang, et al., "Prototype of smart energy router for distribution DC grid," *2015 17th European Conference on Power Electron. and Appl. (EPE'15 ECCE-Europe)*, Geneva, 2015, pp. 1-9.

[15] A. M. Gole, A. Keri, C. Kwankpa, et al., "Guidelines for modelling power electronics in electric power engineering applications," *IEEE Trans. on Power Del.*, vol. 12, no. 1, pp. 505-514, Jan. 1997.

[16] N. Watson and J. Arrillaga. "Power systems electromagnetic transients' simulation," *Institution of Engineering & Technology*, p.448, (2003).

[17] J. Peralta, H. Saad, S. Dennetiere, et al., "Detailed and averaged models for a 401-level MMC–HVDC system," *IEEE Trans. on Power Del.*, vol. 27, no. 3, pp. 1501-1508, Jul. 2012.

[18] G. P. Adam, B. W. Williams, "Half- and full-bridge modular multilevel converter models for simulations of full-scale HVDC links and multiterminal DC grids," *IEEE J. Emerg. Sel. Topics Power Electron.*, vol. 2, no. 4, pp. 1089-1108, Dec. 2014.

[19] J. Xu, Y. Zhao, C. Zhao, et al., "Unified high-speed EMT equivalent and implementation method of MMCs with single-port Submodules," *IEEE Trans. Power Del.*, vol. 34, no. 1, pp. 42-52, Feb. 2019.

[20] J. Xu, S. Fan, C. Zhao, et al., "High-speed EMT modelling of MMCs with arbitrary multiport submodule structures using generalized Norton equivalents," *IEEE Trans. Power Del.*, vol. 33, no. 3, pp. 1299-1307, Jun. 2018.

[21] R. Yin, M. Shi, W. Hu, et al., "An accelerated model of modular isolated DC/DC converter used in offshore DC wind farm," *IEEE Trans. Power Electron.*, vol. 34, no. 4, pp. 3150-3163, Apr. 2019.

[22] T. Zhao, J. Zeng, S. Bhattacharya, et al., "An average model of solid-state transformer for dynamic system simulation," *2009 IEEE Power & Energy Society General Meeting, Calgary, AB*, 2009, pp. 1-8,

[23] S. Ouyang, J. Liu, X. Wang, et al., "The average model of a three-phase three-stage power electronic transformer," *2014 International Power

Electron. Conference (IPEC-Hiroshima 2014 - ECCE ASIA), *Hiroshima*, 2014, pp. 2815-2820.

[24] J. Xu, C. Gao, J. Ping, et al., "High-speed electromagnetic transient (EMT) equivalent modelling of power electronic transformers," *IEEE Trans. Power Del.*, vol. 36, no. 2, pp. 975-986, Apr. 2021.

[25] N. Balabanian, T. A. Bickart, S. Seshu, et al., "Electrical network theory." New York: Wiley, 1969. Print.

[26] C. Gao, M. Feng, J. Ding, et al., "Enhanced Equivalent Model of MMC-Based Power Electronic Transformer," *2020 4th International Conference on HVDC (HVDC)*, Xi'an, China, 2020, pp. 628-633.

[27] PSCAD X4 user's guide, *Winnipeg, MB, Canada: Manitoba Research Center*, 2009.

[28] K. Strunz and E. Carlson, "Nested fast and simultaneous solution for time-domain simulation of integrative power-electric and electronic systems," IEEE *Trans. Power Del.*, vol. 22, no. 1, pp. 277-287, Jan. 2007.

[29] B. Shi, Z. Zhao and Y. Zhu, "Piecewise analytical transient model for power switching device commutation unit," *IEEE Trans. Power Electron.*, vol. 34, no. 6, pp. 5720-5736, Jun. 2019.

[30] M. Salimi, A. M. Gole, R. P. Jayasinghe, "Improvement of transformer saturation modeling for electromagnetic transient programs," *International Conference on Power Systems Transients (IPST2013)*, *Vancouver, Canada*, 2013.

[31] J. Xu, H. Ding, S. Fan, et al., "Enhanced high-speed electromagnetic transient simulation of MMC-MTdc grid," *International Journal of Electrical Power & Energy Systems.*, 2016, 83 (dec.): 7-14.

[32] F. An, B. Zhao, J. Wang, et al., "An adaptive control method of DC transformers imitating AC transformers for flexible DC distribution application," *2020 IEEE Applied Power Electronics Conference and Exposition (APEC)*, New Orleans, LA, USA, 2020, pp. 332-337.

[33] H. Zhang, Y. Li, Z. Li, et al., "Model predictive control of input-series output-parallel dual active bridge converters-based DC transformer," *IET Power Electron.*, vol. 13, no. 6, pp. 1144-1152, Apr. 2020.

Chenxiang Gao was born in Shanxi, China. He received the B.S. degrees in the Power system and its automation from North China Electric Power University (NCEPU) in 2019. Currently, he working towards the Master degree with NCEPU. His research interests include the electromagnetic transient (EMT) equivalent modelling of MMC-HVDC and solid-state transformers (SST) in DC Grid.

Moke Feng was born in Sichuan, China. He received the B.S. degree in power system and automation from NCEPU in 2017. Currently he is a doctoral student at NCEPU. His research interests include HVDC system and EMT modelling of power electronic converters.

Jiangping Ding was born in Jiangxi, China. She received the B.S. degree in power systems and its automation and the Master. degree in electrical engineering from North China Electric Power University, Beijing, China, in 2018 and 2021, respectively. In July 2021, she joined Guangzhou Power Supply Bureau Co., Ltd. as an engineer.

Hang Zhang was born in Hebei, China, in 1991.He received the B.S. degree in electrical engineering from Shijiazhuang Railway University, Hebei, China, in 2015 and the Ph.D. degree in power electronics and power drives with the Institute of Electrical Engineering, Chinese Academy of Sciences, Beijing, China in 2020. Since 2020, he has been with the Key Laboratory of Power Electronics and Electric Drive, Institute of Electrical Engineering, Chinese Academy of Sci-

ences, where he is currently an Assistant Research Fellow. His research interests include circuit topology, analysis, and control of high-power electronic converters, especially its applications in high- or medium-voltage direct current fields.

Jianzhong Xu (M'14-SM'19) was born in Shanxi, China. He received the B.S. and Ph.D. degrees from North China Electric Power University (NCEPU) in 2009 and 2014 respectively. Currently, he is an Associate Professor and Ph.D. Supervisor of the State Key Laboratory of Alternate Electrical Power System with Renewable Energy Sources, North China Electric Power University, China, where he obtained his Ph.D. degree in 2014. From 2012 to 2013 and 2016 to 2017, he was a Visiting Ph.D. student and Post-Doctoral Fellow at the University of Manitoba, Canada. He is an Associate Editor of the CSEE Journal of Power and Energy Systems. He is now working on the Electromagnetic Transient (EMT) equivalent modelling, fault analysis and protection of HVDC Grids.

Dr. Xu has published 24 IEEE Transaction/Journal papers and 4 of them are 'Scopus Top 1% highly cited paper', Dr. Xu also serves as reviewers of 10 IEEE/IET journals and 9 Chinese journals.

Chengyong Zhao (M'05-SM'15) was born in Zhejiang, China. He received the B.S., M.S. and Ph.D. degrees in power system and its automation from NCEPU in 1988, 1993 and 2001, respectively. He was a Visiting Professor at the University of Manitoba from Jan. 2013 to Apr. 2013 and Sep. 2016 to Oct. 2016. Currently, he is a Professor at the School of Electrical and Electronic Engineering, NCEPU. His research interests include HVDC system and DC grid.

Zixin Li (SM'08) was born in Hebei, China, in 1981. He received the B.Eng. degree in industry automation from the North China University of Technology, Beijing, China, in 2005 and the Ph.D. degree (Hons.) in power electronics and electric drives from the Institute of Electrical Engineering, Chinese Academy of Sciences, Beijing, in 2010. Since 2010, he has been with the Institute of Electrical Engineering, Chinese Academy of Sciences, where he is currently a Professor. He is also a Posts Professor with the University of Chinese Academy of Sciences, Beijing, China. He has authored or coauthored more than 100 academic articles and holds more than 20 invention patents in China. His research interests include circuit topology, modulation, control, and analysis of power converters, especially multilevel converters in high-power fields.

Professor Li is an Associate Editor of the IEEE Transactions on Power Electronics, the IET High Voltage, and the Journal of Power Electronics. He was a recipient of the IEEE Power Electronics Society Richard M. Bass Outstanding Young Power Electronics Engineer Award of 2015 for his contributions to multilevel and HVDC converters. He was selected as fellow of the Institution of Engineering and Technology (FIET) in 2019.

Gen Li (M'18) received the B.Eng. degree in electrical engineering from Northeast Electric Power University, Jilin, China, in 2011, the M.Sc. degree in power engineering from Nanyang Technological University, Singapore, in 2013 and the Ph.D. degree in electrical engineering from Cardiff University, Cardiff, U.K., in 2018.

From 2013 to 2016, he was a Marie Curie Early-Stage Research Fellow funded by the European Commission's MEDOW project. He has been a Visiting Researcher at China Electric Power Research Institute and Global Energy Interconnection Research Institute, Beijing, China, at Elia, Brussels, Belgium and at Toshiba International (Europe), London, U.K. He has been a Research Associate at the School of Engineering, Cardiff University since 2017. His research interests include control and protection of HVDC and MVDC technologies, power electronics, reliability modelling and evaluation of power electronics systems.

Dr. Li is a Chartered Engineer in the U.K. He is an Associate Editor of the CSEE Journal of Power and Energy Systems. He is an Editorial Board Member of CIGRE ELECTRA. His Ph.D. thesis received the First CIGRE Thesis

Award in 2018. He is the Vice-Chair of IEEE PES Young Professionals and the Technical Panel Sectary of CIGRE B5 Protection and Automation.